Pattern-Distortion Technique: Using Liquid-Lens Magnification to Extract Volumes of Individual Droplets or Bubbles within Evaporating Two-Dimensional Arrays

J.J. Kilbride, K.E. Fagg, F.F. Ouali, and D.J. Fairhurst*
SOFT Group, School of Science and Technology, Nottingham Trent University, Clifton Lane, Nottingham NG11 8NS, United Kingdom

(Received 14 October 2022; revised 16 January 2023; accepted 15 February 2023; published 11 April 2023)

We present an experimental "pattern-distortion" (PD) technique which connects the shape of a liquid lens to its magnification. We demonstrate how to optimize the technique for arbitrary droplet sizes and optical configurations, and demonstrate its widespread utility in three distinct situations. Firstly, we consider multiple sessile droplets. Although ubiquitous in nature, understanding of their complex interactions is limited, partly due to experimental limitations in determining individual droplet volumes for arbitrary configurations. We use the PD technique to overcome these limitations, and we find excellent agreement between our experimental data and three recent theoretical models. Secondly, we show how our technique can be used to inform the design of liquid lenses. Thirdly, we extend the method to composite droplets systems, using it to extract the size of an air bubble trapped inside a liquid droplet.

DOI: 10.1103/PhysRevApplied.19.044030

I. INTRODUCTION

The geometry of liquids [1–5] and surfaces [6] can be determined remotely using their optical properties. In this work we present a simple optimized droplet lensing technique which analytically connects the shape of a droplet to the magnification. We employ a transfer matrix method (as described in Hecht [7] and Pedrotti *et al.* [8]) to relate the optical distortion of a pattern placed beneath each droplet to its volume. This simple connection between magnification and droplet shape is of particular interest to the development of liquid lenses. Much of the existing work focuses on methods of controlling the position of liquid interfaces (see Zhu *et al.* [9] for a review) but not the effect this control has on the optical properties. We demonstrate the range of magnifications which can be achieved by adapting the shape of a single droplet, helping inform liquid lens design. After validating the method by comparing against traditional profile imaging, we apply the technique to understanding the dynamics of evaporating multiple droplets.

The evaporation of a single droplet has been thoroughly studied and accurate predictions exist for the evaporative fluxes [10–12], internal flow [13], and heat transfer [14]. However, more often droplets evaporate in groups: as sweat on skin, raindrops on surfaces, or condensing from breath. There are many applications of these interactions, including ink-jet printing, spray coating, and limiting viral transmission. In these dense arrays the droplets interact with their neighbors, significantly reducing their individual evaporation rates. Understanding these interactions has been the focus of several recent theoretical publications [15–20] which relate the diffusion-limited interactions in the vapor phase (shielding effect) to droplet size, proximity and position within the array. Initial experimental work using interferometry [21] and side imaging [22] to measure evaporation rates found good agreement with the models of Fabrikant and Wray *et al.* [16,23] and Masoud *et al.* [17]. However, inherent challenges and limitations of these experimental techniques prevent further validation, as side cameras cannot view obscured droplets in the center of two-dimensional arrays and interferometers require complex alignment, measuring only changes in droplet height. As a result, experimental work has fallen behind the theory. Our method facilitates the acceleration of experimental work in this area informing much needed guidance for improving the analytical models, as it provides significant advantages over previous techniques including: a much simpler implementation; the ability to measure absolute volumes; and distinguishing between condensation and evaporation. We implement the pattern-distortion (PD) technique to perform experiments and provide comparisons of the different theoretical models, extending our previous work [24] using the method to evaluate the performance of the predictions of Masoud *et al.* [17]. We also demonstrate how our method can be extended to determine the properties of composite droplets, such as those containing bubbles or emulsions [25].

*Corresponding Author: david.fairhurst@ntu.ac.uk

II. THE PATTERN-DISTORTION TECHNIQUE

A. Transfer Matrix Optics

In order to quantify how the magnification by a droplet is related to its geometry we apply an optical transfer matrix method. The method traces paraxial rays through an optical system by combining matrices corresponding to translations through a uniform medium of thickness d, or refractions at an interface, with a radius of curvature r between two refractive indices n_1 and n_2. For our sessile droplet optical system [see Fig. 1(a)] there are four translations (through the air under the substrate d_1, the substrate d_2, the droplet height h and to the image plane $d_3 - h$) and three refractions at the interfaces between them, resulting in seven matrices:

$$\chi = \begin{pmatrix} 1 & d_3 - h \\ 0 & 1 \end{pmatrix} \begin{pmatrix} 1 & 0 \\ \frac{n_L - n_G}{r n_G} & \frac{n_L}{n_G} \end{pmatrix} \begin{pmatrix} 1 & h \\ 0 & 1 \end{pmatrix} \begin{pmatrix} 1 & 0 \\ 0 & \frac{n_S}{n_L} \end{pmatrix} \times \begin{pmatrix} 1 & d_2 \\ 0 & 1 \end{pmatrix} \begin{pmatrix} 1 & 0 \\ 0 & \frac{n_G}{n_S} \end{pmatrix} \begin{pmatrix} 1 & d_1 \\ 0 & 1 \end{pmatrix} = \begin{pmatrix} \chi_{11} & \chi_{12} \\ \chi_{21} & \chi_{22} \end{pmatrix}. \quad (1)$$

Here n_G, n_S, n_L denote the refractive indices of the gas, substrate, and liquid, respectively. Matrix multiplication of Eq. (1) reduces χ to a single 2×2 matrix describing how points in the object plane (y_{obj}) are mapped onto the image plane (y_{im}). For an in-focus image to form, all rays leaving a point on the object must converge to a single point in the image plane. This means y_{im} cannot depend on the ray's initial angle (ϕ_{obj}), implying element χ_{12} must be zero. We therefore recognize that $\chi_{11} = y_{\text{im}}/y_{\text{obj}}$ is the linear magnification (M) of the optical system. These conditions make it possible to derive an expression for the radius of curvature of the droplet's upper surface (r) in terms of known quantities:

$$M = \frac{r n_G}{r n_G - \left(d_1 + \frac{h n_G}{n_L} + \frac{d_2 n_G}{n_S}\right)(n_G - n_L)}. \quad (2)$$

For a more detailed derivation of Eq. (2) and description of the matrix transfer method see Appendix A. If the droplet is undistorted by gravity (i.e. when the Bond number is small, $\text{Bo} = \rho g h^2/\gamma \ll 1$), its shape can be considered a spherical cap and r in Eq. (2) can be related to the height h and base radius a, resulting in

$$M = \frac{h^2 + a^2}{(2n-1)h^2 - 2nlh + a^2}, \quad (3)$$

where

$$n = \frac{n_G}{n_L}, \quad (4a)$$

$$l = \frac{n_L - n_G}{n}\left(\frac{d_1}{n_G} + \frac{d_2}{n_S}\right). \quad (4b)$$

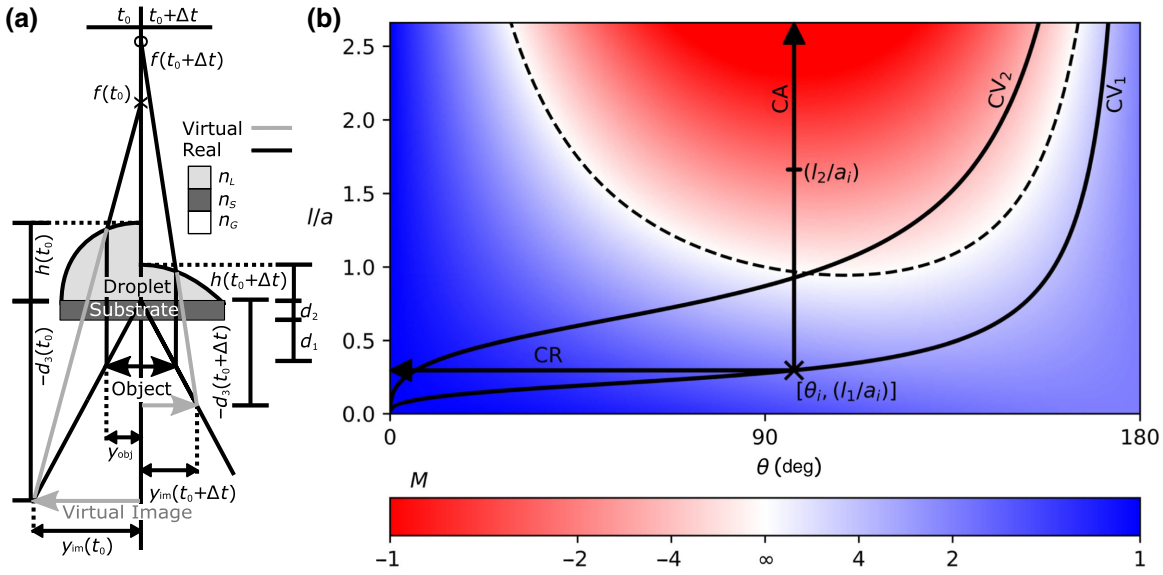

FIG. 1. (a) Diagram tracing real (black) and virtual (gray) ray paths from the pattern (d_1, n_G), through the substrate (d_2, n_S) and droplet (h,n_L), to the (virtual) image plane (d_3), for a time t_0 (left) and $t_0 + \Delta t$ (right, of the optical axis). y_{im} is the height of the image formed and f is the focal point of the droplet. (b) The magnification M mapped over contact angle (θ) and l/a. The dashed line indicates $M = \infty$. The black cross at $[\theta_i, (l_1/a_i)]$ indicates the approximate initial position of the droplets in Fig. 2. The vertical and horizontal lines show the evolution of M for CA and CR evaporation, respectively. The curved lines indicate the magnifications which can be traversed by an actuated liquid lens of constant volume $CV_1 = 10$ μL and $CV_2 = 0.1$ μL.

The term l has units of length and captures the various optical and geometric parameters of the setup. By expressing the droplet height in terms of the contact angle θ, Eq. (3) can be rewritten as

$$M = \frac{\tan^2\left(\frac{\theta}{2}\right) + 1}{(2n-1)\tan^2\left(\frac{\theta}{2}\right) - 2n\left(\frac{l}{a}\right)\tan\left(\frac{\theta}{2}\right) + 1}. \quad (5)$$

In Fig. 1(b), we use Eq. (5) to plot the calculated values of M for a range of l/a and θ values, which can be used to optimize the experimental setup to provide the largest sensitivity to changes in the droplet's shape. The white region represents high magnification, with the black dashed line indicating an infinitely magnified image, determined mathematically by setting the denominator in Eq. (5) equal to zero. The length scale l emerges as the radius of a droplet with contact angle $\theta = 90^\circ$ that forms an image with infinite magnification.

B. Optimization

To experimentally measure the magnification, an object placed beneath each droplet must be imaged from above using a fixed top-down camera. For repeating patterns the maximum absolute magnification $|M^+|$ should be chosen to ensure each droplet has at least one measurable dot initially within the analyzed region of interest (ROI). The ROI should be centered on the droplet apex, avoiding the distorted features near the contact line. The values d_1 and d_2, contained within the parameter l, can be used to manipulate the initial magnification. The sign of M^+ corresponds to whether a real (inverted) or virtual (upright) image is formed and makes it possible to prevent droplets crossing the dashed line in Fig. 1(b), when the magnification will become too large to be analyzed. The choice of which side of the dashed line an experiment should start is determined by the droplet's mode of evaporation: for a constant contact radius (CR), evaporation trajectories move from right to left in Fig. 1(b) from an initial coordinate $[\theta_i, l_1/a_i]$. To avoid crossing into the red region, l can be selected to place the droplet in the blue region (forming a virtual image). It can also be utilized to ensure monotonic variation in magnification. For a constant contact angle (CA), evaporation will result in an upward trajectory and therefore a better choice of l in Fig. 1(b) is l_2 commencing in the red region (forming a real image). Figure 1(b) allows optimal design of the experimental setup, tailored to specific droplet geometries. In addition to evaporation experiments, Fig. 1(b) can assist the design of adaptive liquid lenses. The curved solid lines plot the magnification by liquid lenses of constant volume (CV) whose shape is controlled by means of actuation techniques (e.g., electrowetting). The curve CV_1 represents the possible values for a droplet with $V = 3.0$ μL and $l_1 = 3.2 \times 10^{-4}$ mm, which are the experimental values of the droplets presented within the article. The second curve (CV_2) illustrates the possible magnifications for a smaller lens of $V = 0.1$ μL, which is capable of forming both real and virtual images.

III. VALIDATION

In order to validate the technique, a single high-resolution repeating hexagonal dot pattern is used as the object, to avoid the need for alignment of individual features with the center of each droplet. Chrome dots are printed lithographically on soda-lime glass (SL12, JD Photo Data) with a diameter of 100.0 ± 0.4 μm and a pitch of 150 μm with a cumulative accuracy of ±2 μm over 70.7 mm. To ensure the droplets maintain a known circular base radius throughout evaporation, the contact line is pinned. To achieve this, a clean glass slide ($n_S = 1.46$) is covered with polyimide tape and a 10-W UV 355-nm (TRUMPF, SCIII10SL) laser is used to make circular incisions in the tape. The outer part of the tape is then removed and the slide is hydrophobized by spray-coating with Glaco Mirror Coat Zero [SOFT99], baked for 12 minutes at 50°C and left to cure for 10 minutes. Finally, the remaining circular pieces of tape are removed, revealing uncoated hydrophilic glass regions, surrounded by the hydrophobic coating. Controlling the size and position of these circular incisions means bespoke templates can be created which pin the location and contact lines of the droplets for approximately 80% of their drying time.

A deionized water droplet ($n_L = 1.33$) with $a = 1.06 \pm 0.04$ mm, $\theta \approx 97^\circ$ and $V_0 \approx 3$ μL is deposited into the hydrophilic region of the prepared substrate of thickness $d_2 = 1.05 \pm 0.01$ mm with the pattern placed directly beneath ($d_1 = 0$ mm). To prevent air currents the droplets were contained within an acrylic box ($W = 722$ mm, $H = 510$ mm, $D = 473$ mm) with an ambient relative humidity (RH) of 38.2% and temperature (T) of 22.9°C. Images are taken simultaneously by a top charged couple device (CCD) camera with a 0.3× rectilinear lens and side CCD camera with a 4× objective lens to measure the magnification and height, respectively. To extract the magnification from the top images a MATLAB circle detection script (available at github.com/JoeyKilbride/Pattern-Distortion-Technique) was written to place a region of interest over the central portion of each droplet and measure the median diameter of the dots in each frame. This value is divided by the final median diameter, when the droplet has evaporated, to calculate M. By rearranging Eq. (3) the quadratic can be solved for the two roots and M is converted to a height h. The appropriate root can be determined by knowing if the image is virtual/real, as the positive root is the larger/smaller value of h:

$$h = \frac{Mnl \pm \sqrt{(Mnl)^2 - a^2(M(2n-1)-1)(M-1)}}{M(2n-1)-1}. \quad (6)$$

The height determined from top-camera magnification and Eq. (6) (h_{top}) is plotted against the height measured directly by a side camera (h_{side}) in Fig. 2(a). The gray region represents the variation in h_{top} within the uncertainty of the measured base radius. The data agree well with the black line ($h_{\text{top}} = h_{\text{side}}$), confirming the PD technique's ability to capture the shape of the droplet from its magnification. To further validate the PD technique we applied the same method to a three-droplet line. In Fig. 2(b) we again plot h_{top} against h_{side} for the left (L, blue), middle (M, green), and right (R, red) droplets with initial base radii of $a_L = 0.99 \pm 0.03$ mm, $a_M = 1.03 \pm 0.04$ mm, and $a_R = 0.98 \pm 0.05$ mm, respectively, and a center-to-center separation of $4a$. For this multiple droplet system the PD data again agree closely with the side-camera heights for the blue and red series. The slight noncircularity of the middle droplet's contact line results in the topology of the liquid interface diverging from a spherical shape. As a result, the imaged dots become marginally distorted, which causes the minor discrepancy seen in the green series and highlights the sensitivity of the method to the shape of the contact line. This visualization of the droplet heights masks the observed difference in evaporation rate, with the middle droplet taking 11% (about 200 s) longer to evaporate.

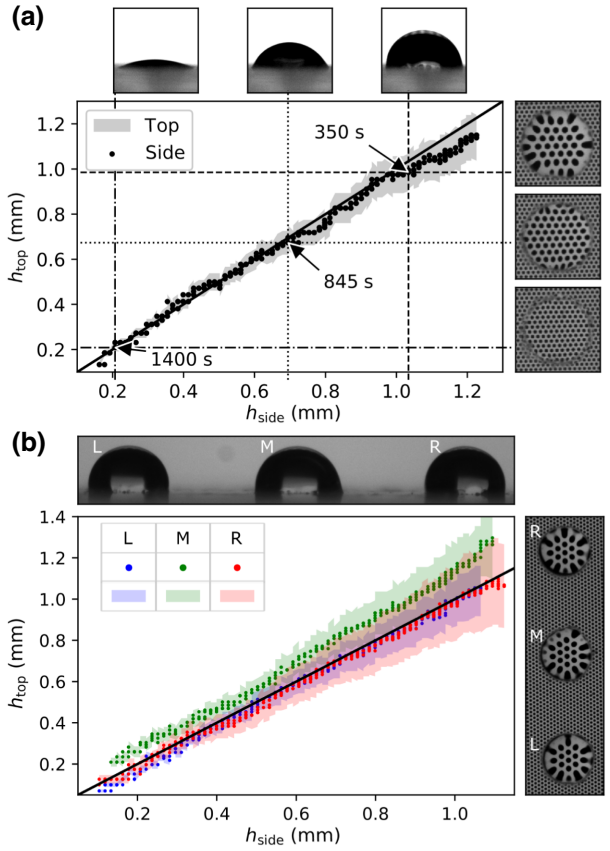

FIG. 2. Height determined by the top camera (h_{top}) by substitution of M into Eq. (6) against side-camera height (h_{side}) for (a) an isolated droplet, where the surrounding insets show three top and side frames during evaporation; (b) three-droplet line with the left (L), middle (M) and right (R) colored blue, green, and red, respectively. The surrounding insets show the first experimental frames from the top and side cameras. The filled regions are the variation in h_{top} due to the uncertainty in the base radius (a).

A. Movement of the image plane

An important experimental consideration is the movement of the image plane, located at $d_3(t)$, along the optical axis during evaporation. This movement can lead to the image of the dots shifting outside the depth of field of the CCD camera, increasing the size of the circle of confusion. The resulting blur in the image makes identifying the size of each droplet ambiguous and gives rise to an uncertainty in M. To investigate the effect of the dot edge becoming defocused, the variation in dot diameter ϵ was measured as it was translated a distance δ from the focal plane of the CCD camera. Figure 3 shows $\epsilon/\epsilon_{\delta=0}$. To compare this to how far the image plane moves as the droplet lens changes shape, the maximum displacement of d_3 for a droplet evaporating in CR mode with $a = 1$ mm, for initial contact angles $\theta_i = 90°, 145°$, and $165°$ is also plotted. It can be seen from the position of the blue bars that for higher values of θ_i it is important to ensure that the dot pattern is perfectly in focus midway through evaporation, in order to minimize the uncertainty. The blue bars are therefore centered on $\delta = 0$ and positioned horizontally at the point of intersection with the defocusing curve of the lens (black data points). The x axis intercept indicated by the dotted blue lines therefore represents the uncertainty in M due to the movement of the image plane. For the droplets used

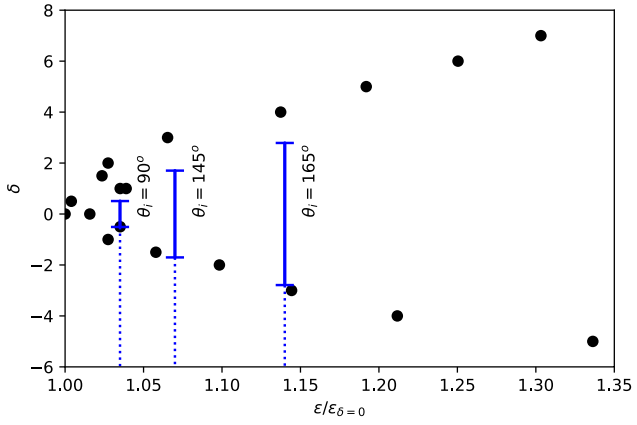

FIG. 3. Variation in normalized dot diameter ($\epsilon/\epsilon_{\delta=0}$) translated a distance δ from the imaging plane of the CCD camera. The blue bars represent the range of movement in the image plane, for complete evaporation from three initial contact angles (θ_i). The bars are positioned horizontally to encompass the maximum magnification data point within this range when centered vertically at $\delta = 0$. The increase in M due to defocusing is therefore indicated by the dashed lines.

in this work, this corresponds to a variation of about 4%. For experiments with $\theta_i > 90^\circ$ this value can be reduced by selecting a lens with a larger depth of field.

IV. IMPLEMENTATION

A. Evaporation in two-dimensional droplet arrays

The PD technique was then used to experimentally measure droplet volumes simultaneously from different configurations which could not have been fully captured with side cameras. Detailed comparisons of these experiments and the theoretical model of Masoud *et al.* [17] are presented by Iqtidar *et al.* [24]. Here we present one of these configurations (a 3×3 droplet square [26]) and use it to make further comparisons with the model of Fabrikant and Wray *et al.* [16,23].

Droplets with volume $V_o = 2.00 \pm 0.25$ μL are deposited onto a prepared substrate to pin the base radii ($a = 0.97 \pm 0.07$ mm) with a center-to-center separation of $3a$, resulting in $\theta_i \approx 90^\circ$. The normalized volume data of each droplet is truncated at the point of depinning and averaged over three repeat experiments. V is then averaged across symmetrical confinement [corners (12 droplets), edges (12 droplets), and centers (three droplets)] and compared in Fig. 4(a) to Fabrikant and Wray *et al.* [16,23] (solid) and Masoud *et al.* [17] (dashed). We normalize t by the time it takes the fastest evaporating droplet to reach half its initial volume t^*. Excellent agreement is obtained with both models, with the slightly closer agreement to Fabrikant and Wray *et al.* [16,23] being explained by our choice of normalization. In Fig. 4(b) we fit the total nine-droplet average volume (V_T) of the array to the theory of Carrier *et al.* [15], which approximates an array to a single superdrop. The radius of the superdrop is calculated from the evaporation rate to be $a_s = 5.13$ mm and is drawn centered over the first experimental frame from the top camera, in the inset, closely aligning with the outer extent of the array.

B. Composite Lenses

To demonstrate the wider applicability of the technique we next consider a composite droplet lens. By making a slight modification to the matrices in Eq. (1) (see Appendix B for details) we are able to use the PD technique to determine the size of a bubble trapped at the apex of a droplet. To do this we first measure the magnification of dots just outside the bubble to obtain the height of the droplet, h, by substituting into Eq. (6). Then by analyzing the reduced magnification [depicted in Fig. 5(a)(i)], caused by the concave lower interface of the bubble, we calculate a predicted value for its radius of curvature of $r_B = 0.29 \pm 0.06$ mm, entirely from top-camera measurements. If the bubble is assumed spherical this value can be verified by using a side camera to infer r_B. To do this we measure the change in volume of the droplet just before [Fig. 5(b)(i)] and just after the bubble pops [Fig. 5(b)(ii)], yielding $r_B = 0.35 \pm 0.12$ mm. Comparing these two values demonstrates that the PD technique can successfully be applied to composite lenses [25] as well as to measure and study bubbles. Figure 5(a) also shows how the precision in the technique can be significantly enhanced for applications which do not require a large field of view when a higher magnification lens is used.

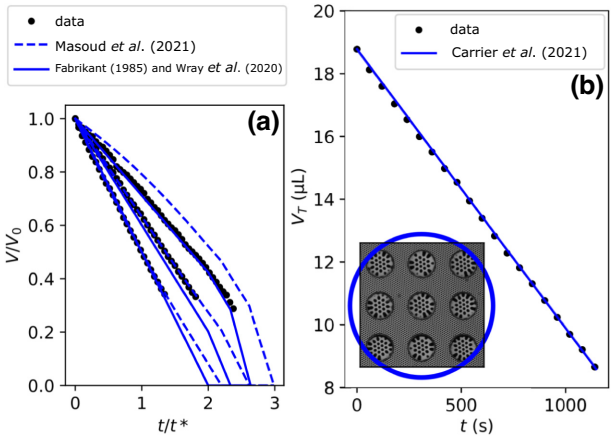

FIG. 4. Experimental data of a 3×3 square compared (a) to the predictions of Fabrikant and Wray *et al.* [16,23] (solid) and Masoud *et al.* [17] (dashed) of the normalized volume (V/V_0) against normalized time (t/t^*). (b) to the radius ($a_s = 5.13$ mm) of a superdrop (blue circle) obtained by fitting the total nine-droplet volume (V_T) to Carrier *et al.* [15].

V. CONCLUSION

To conclude, we proposed and validated an optimized pattern-distortion technique relating the shape of a liquid lens to its magnification. We then applied the method to measure the absolute volumes for up to nine droplets in a two-dimensional array, which could not have been captured with previous techniques. We then used these measurements to compare the predictions of the theoretical models proposed by Fabrikant and Wray *et al.* [16,23], Masoud *et al.* [17], and Carrier *et al.* [15], finding excellent agreement with all three. The simplicity of our PD method means that this approach could be implemented using two mobile phones: the screen of one displaying a high-resolution and adaptable pattern and the camera of the second recording the magnification of the pixel features. The method could also replace interferometric characterization of liquid lens arrays [27] and be used to monitor droplets where both evaporation and condensation are occurring. Additionally, we illustrated how our work can be used to assist in the design of liquid lenses. Finally, we used the PD technique to analyze composite liquid lenses, using it to extract the size of an air bubble inside

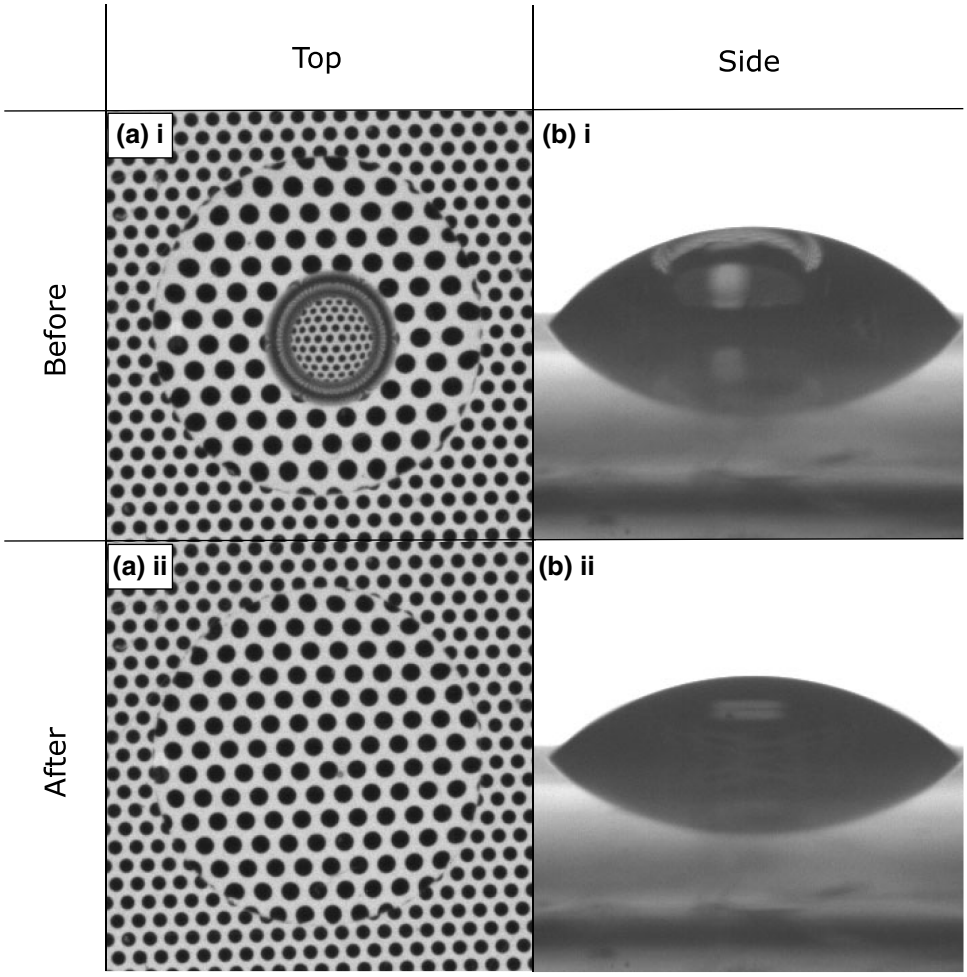

FIG. 5. (a) Top- and (b) side-camera view of a droplet with an air bubble trapped at its apex, before (i) and after (ii) popping, imaging a pattern place beneath.

a liquid droplet. Future work could include applying our work to improve the algorithms used to remove the optical distortion caused by raindrops on security cameras [28].

ACKNOWLEDGMENTS

This research was funded by the Nottingham Trent University Vice Chancellor's Scholarship and a Santander BECAS award. We would also like to thank Dr. Magdalena Patel, Mr. Josh Parker, and Dr. Akhshay Bhadwal for useful discussions and the Medical Technologies and Innovation Facility (MTIF) for access to the laser cutter.

APPENDIX A: TRANSFER MATRIX METHOD

Consider a ray which has reached an interface some distance y_i above the optical axis traveling at some angle ϕ_i. The ray will refract according to Snell's law, resulting in a new angle ϕ_f. The ray will then translate some distance d through the medium at ϕ_f, reaching a new position y_f. These refraction and translation events can be represented (in the small-angle, paraxial ray limit) by matrix operators

$$\mathbf{T} = \begin{pmatrix} 1 & d \\ 0 & 1 \end{pmatrix} \tag{A1}$$

and

$$\mathbf{R} = \begin{pmatrix} 1 & 0 \\ \frac{n_i - n_f}{r n_i} & \frac{n_i}{n_f} \end{pmatrix}, \tag{A2}$$

which transform y and ϕ, dependent on the initial (n_i) and final (n_f) refractive indices of the materials and the interface's local radius of curvature (r) [7,8]. Composite optical systems can therefore be described by a series of translation and refraction matrices. By multiplication, the series of matrices can be reduced to a single 2×2 system operator (χ), which can be used to map rays leaving the object plane ($y_{\text{obj}}, \phi_{\text{obj}}$) to rays arriving at the image plane

$(y_{\text{im}}, \phi_{\text{im}})$:

$$\begin{pmatrix} y_{\text{im}} \\ \phi_{\text{im}} \end{pmatrix} = \chi \begin{pmatrix} y_{\text{obj}} \\ \phi_{\text{obj}} \end{pmatrix} = \begin{pmatrix} \chi_{11} & \chi_{12} \\ \chi_{21} & \chi_{22} \end{pmatrix} \begin{pmatrix} y_{\text{obj}} \\ \phi_{\text{obj}} \end{pmatrix}. \tag{A3}$$

Multiplying out Eq. (A3) into its underlying system of linear equations yields

$$y_{\text{im}} = \chi_{11} y_{\text{obj}} + \chi_{12} \phi_{\text{obj}}, \tag{A4}$$

$$\phi_{\text{im}} = \chi_{21} + \chi_{22} \phi_{\text{im}}. \tag{A5}$$

In order for an image to form, all rays from the object plane must come to a single point on the image plane. Therefore, the final height of each ray on the image plane y_{im} cannot depend on the initial angle of the rays at the object plane ϕ_{obj}. Consequently, the element χ_{12} is equal to zero. For our situation of seven matrices this leads to

$$\chi_{12} = d_1 + (d_3 - h)\left[\frac{(n_L - n_G)(d_1 + \frac{h n_G}{n_L} + \frac{d_2 n_G}{n_S})}{r n_G} + 1\right] + \frac{h n_G}{n_L} + \frac{d_2 n_G}{n_S} = 0. \tag{A6}$$

Rearranging results in an expression for the position of the image plane,

$$d_3 = h - \left[\frac{r n_G \left(\frac{d_1}{n_G} + \frac{h}{n_L} + \frac{d_2}{n_S}\right)}{(n_L - n_G)\left(\frac{d_1}{n_G} + \frac{h}{n_L} + \frac{d_2}{n_S}\right) + r}\right]. \tag{A7}$$

The term χ_{11} in Eq. (A4) represents the linear magnification of the system:

$$\frac{y_{\text{im}}}{y_{\text{obj}}} = \chi_{11} = M = \frac{(d_3 - h)(n_L - n_G)}{r n_G} + 1. \tag{A8}$$

Equation (A7) can be used to substitute for the unknown d_3, which after rearrangement yields an expression relating M to the radius of curvature of the droplet's interface in terms of known distances d_1 and d_2 and refractive indices n_L, n_G, and n_S, as given by Eq. (2) in the main text.

APPENDIX B: DROPLET-BUBBLE COMPOSITE LENS

To apply pattern distortion to a droplet-bubble composite lens the matrices in Eq. (1) (in the main text) need to be adapted. The distances in the first and third translation matrices are adjusted by the diameter of the bubble $(2r_B)$, and the radius of curvature in the second refraction matrix is now $-r_B$ due to the bubble's concave surface, rather than the convex surface of the droplet $+r$:

$$\chi = \begin{pmatrix} 1 & d_3 - h + 2r_B \\ 0 & 1 \end{pmatrix} \begin{pmatrix} 1 & 0 \\ \frac{n_L - n_G}{r_B n_G} & \frac{n_L}{n_G} \end{pmatrix} \begin{pmatrix} 1 & h - 2r_B \\ 0 & 1 \end{pmatrix} \times \begin{pmatrix} 1 & 0 \\ 0 & \frac{n_S}{n_L} \end{pmatrix} \begin{pmatrix} 1 & d_2 \\ 0 & 1 \end{pmatrix} \begin{pmatrix} 1 & 0 \\ 0 & \frac{n_G}{n_S} \end{pmatrix} \begin{pmatrix} 1 & d_1 \\ 0 & 1 \end{pmatrix} = \begin{pmatrix} \chi_{11} & \chi_{12} \\ \chi_{21} & \chi_{22} \end{pmatrix}. \tag{B1}$$

The upper surface of the bubble was omitted as it was assumed to be uniform and thin, thus having an insignificant effect on the optics. As a result, mathematically the rays refract at the lower interface of the bubble and then translate directly to the image plane. An equation relating M to r_B was then derived as described previously.

To create the droplet-bubble composite liquid lens, a droplet of deionized water with a volume of 1.3 μL was deposited onto a clear acrylic substrate of thickness $d_2 = 0.8 \pm 0.01$ mm and refractive index $n_S = 1.489$. A bubble of air was then injected inside the droplet using a pipette. The droplet-bubble was recorded simultaneously with top [Fig. 5(a)] and side [Fig. 5(b)] cameras until the bubble popped and the magnifications were extracted from the frames directly before Fig. 5(i) and after Fig. 5(ii).

[1] K. H. Kang, S. J. Lee, C. M. Lee, and I. S. Kang, Quantitative visualization of flow inside an evaporating droplet using the ray tracing method, Meas. Sci. Technol. **15**, 1104 (2004).

[2] H. Ren, S. Xu, and S.-T. Wu, Effects of gravity on the shape of liquid droplets, Opt. Commun. **283**, 3255 (2010).

[3] D. Geiger, K. Geiger, T. Neckernuss, O. Marti, and M. Amirkhani, Measurement of contact angles of microscopic droplets by focal length method, Rev. Sci. Instrum. **88**, 083701 (2017).

[4] H. Cha, J. Ma, Y. S. Kim, L. Li, L. Sun, J. Tong, and N. Miljkovic, In situ droplet microgoniometry using optical microscopy, ACS Nano **13**, 13343 (2019).

[5] J. Freeland, V. R. Krishnamurthi, and Y. Wang, Learning the lens equation using water and smartphones/tablets, Phys. Teacher **58**, 360 (2020).

[6] F. Moisy, M. Rabaud, and K. Salsac, A synthetic schlieren method for the measurement of the topography of a liquid interface, Exp. Fluids **46**, 1021 (2009).

[7] E. Hecht, Optics 4th edition, Optics 4th edition by Eugene Hecht Reading (2001).

[8] F. L. Pedrotti, L. M. Pedrotti, and L. S. Pedrotti, *Introduction to Optics* (Cambridge University Press, Cambridge, 2017), 399.

[9] G.-P. Zhu, J.-F. Yao, S.-H. Wu, and X.-D. Zhang, Actuation of adaptive liquid microlens droplet in microfluidic devices: A review, Electrophoresis **40**, 1148 (2019).

[10] R. D. Deegan, O. Bakajin, T. F. Dupont, G. Huber, S. R. Nagel, and T. A. Witten, Capillary flow as the cause

of ring stains from dried liquid drops, Nature **389**, 827 (1997).
[11] Y. O. Popov, Evaporative deposition patterns: spatial dimensions of the deposit, Phys. Rev. E **71**, 036313 (2005).
[12] R. G. Larson, Transport and deposition patterns in drying sessile droplets, AIChE J. **60**, 1538 (2014).
[13] A. M. J. Edwards, P. S. Atkinson, C. S. Cheung, H. Liang, D. J. Fairhurst, and F. F. Ouali, Density-Driven Flows in Evaporating Binary Liquid Droplets, Phys. Rev. Lett. **121**, 184501 (2018).
[14] P. Sáenz, K. Sefiane, J. Kim, O. Matar, and P. Valluri, Evaporation of sessile drops: a three-dimensional approach, J. Fluid Mech. **772**, 705 (2015).
[15] O. Carrier, N. Shahidzadeh-Bonn, R. Zargar, M. Aytouna, M. Habibi, J. Eggers, and D. Bonn, Evaporation of water: evaporation rate and collective effects, J. Fluid Mech. **798**, 774 (2016).
[16] A. W. Wray, B. R. Duffy, and S. K. Wilson, Competitive evaporation of multiple sessile droplets, J. Fluid Mech. **884**, A45 (2020).
[17] H. Masoud, P. D. Howell, and H. A. Stone, Evaporation of multiple droplets, J. Fluid Mech. **927**, R4 (2021).
[18] D. J. Fairhurst, Predicting evaporation rates of droplet arrays, J. Fluid Mech. **934**, F1 (2022).
[19] S. Tonini and G. Cossali, Analytical modeling of the evaporation of sessile drop linear arrays, Phys. Rev. E **105**, 054803 (2022).
[20] Q. Liu, R. Lu, Y. Qiao, F. Zhao, and S. Tan, Analysis of the correction factors and coupling characteristics of multi-+droplet evaporation, Int. J. Heat Mass Transf. **195**, 123138 (2022).
[21] A. M. Edwards, J. Cater, J. J. Kilbride, P. Le Minter, C. V. Brown, D. J. Fairhurst, and F. F. Ouali, Interferometric measurement of co-operative evaporation in 2d droplet arrays, Appl. Phys. Lett. **119**, 151601 (2021).
[22] H. Chen, Q. An, H. Zhang, C. Li, H. Fang, and Z. Yin, Predicting the lifetimes of evaporating droplets in ordered arrays, Phys. Fluids **34**, 082010 (2022).
[23] V. Fabrikant, On the potential flow through membranes, Z. für Angew. Math. Phys. ZAMP **36**, 616 (1985).
[24] A. Iqtidar, J. J. Kilbride, F. F. Ouali, D. J. Fairhurst, H. A. Stone, and H. Masoud, Drying dynamics of sessile-droplet arrays, Phys. Rev. Fluids **8**, 013602 (2023).
[25] S. Nagelberg, L. D. Zarzar, N. Nicolas, K. Subramanian, J. A. Kalow, V. Sresht, D. Blankschtein, G. Barbastathis, M. Kreysing, and T. M. Swager, *et al.*, Reconfigurable and responsive droplet-based compound micro-lenses, Nat. Commun. **8**, 1 (2017).
[26] See supplemental material at http://link.aps.org/supplemental/10.1103/PhysRevApplied.19.044030 for video of the evaporation of the 3 by 3 droplet square.
[27] S. Grilli, L. Miccio, V. Vespini, A. Finizio, S. De Nicola, and P. Ferraro, Liquid micro-lens array activated by selective electrowetting on lithium niobate substrates, Opt. Express **16**, 8084 (2008).
[28] R. Qian, R. T. Tan, W. Yang, J. Su, and J. Liu, in *Proceedings of the IEEE conference on computer vision and pattern recognition* (2018), p. 2482.